Effect of Water Vapour Partial Pressure on the Chromia (Cr_2O_3)-Based Scale Stability

Shooka Mahboubi[1], Gianluigi A. Botton[2], Hatem S. Zurob[3], and Joey R. Kish[4,*]

[1]*Shooka Mahboubi, mahbos@mcmaster.ca (905) 525-9140, ext. 27226*

[2]*Gianluigi A. Botton: gbotton@mcmaster.ca, (905) 525-9140, ext. 24767*

[3]*Hatem S. Zurob: zurobh@mcmaster.ca (905)525-9140, ext. 23515*

[4,*]*Joey R. Kish: corresponding author, kishjr@mcmaster.ca (905)525-9140, ext. 21492*

Department of Materials Science and Engineering, McMaster University, 1280 Main Street West, Hamilton, ON, CA

Abstract

The kinetics of the Cr_2O_3-based scale oxidation and volatilization were studied in the presence of water vapour (H_2O). A commercial Cr_2O_3-based scale forming Type 310S stainless steel was examined at the ambient pressure (0.1 MPa) and 550 ºC in relatively low and high H_2O containing environments of air-10% H_2O and air-70% H_2O, respectively. The increase in the partial pressure of H_2O (p_{H_2O}) from 10% to 70% resulted in transition of the oxidation and volatilization kinetics from the parabolic rate law in air-10% H_2O to the paralinear rate law in air-70% H_2O. The kinetics transition was attributed to the increase in the Cr loss rate from the base scale after coupons exposure in air-70% H_2O. The significant role of Mn alloying element in the base scale protectiveness was discussed in the context of the Cr_2O_3-based scale stability.

Keywords: Kinetics, Cr_2O_3-based scale, Oxidation, Volatilization, Water vapour, Type 310S stainless steel, Alloying element

1. Introduction

High-temperature oxidation and oxide scale volatilization in oxygen (O_2) and H_2O containing environments are unavoidable phenomena that limit the performance of the corrosion-resistant alloys used as structural components for steam-generating applications such as: steam boiler power plants, solid oxide fuel cells, nuclear reactors and geothermal power plants.[1-8] One method to increase the steam oxidation resistance of the alloy structural components is to modify the composition to form a protective external Cr_2O_3-based scale.[9-12] It is well-known that increasing an alloy Cr-content can enhance the formation of a protective external Cr_2O_3-based scale.[9-12] Even though the increased Cr content in an austenitic Fe-Cr-Ni alloy is desirable from the Cr_2O_3-based scale formation perspective, one major concern exists. The Cr_2O_3 scale is known to form volatile Cr species such as $CrO_2(OH)$, $Cr(OH)_3$, CrO_3, $CrO(OH)_2$ and $CrO_2(OH)_2$.[13-16] Thermodynamic calculations of volatile Cr species partial pressures have shown that the most dominant phase that is responsible for oxide scale breakaway at temperatures below ~ 900 °C is Cr oxy-hydroxide: $CrO_2(OH)_2$ (equation 1), whereas at temperatures above ~ 900 °C, CrO_3 and $CrO_2(OH)$ species form significantly as well.[14]

$$\frac{1}{2}Cr_2O_{3_{(s)}} + H_2O_{(g)} + \frac{3}{4}O_{2_{(g)}} = CrO_2(OH)_{2_{(g)}} \quad (1)$$

It is known that the high Cr-containing alloys oxidation and formation of an external protective Cr_2O_3-based scale follows a parabolic rate law as such scale reduces further ion diffusion, therefore decreases the oxidation reaction rate.[1] Oxidation kinetics of the Cr_2O_3-based scale forming alloys in the presence of H_2O and any possible transition in the reaction kinetics during scale volatilization, however, is not well understood yet.

The volatile species during the Cr_2O_3-based scale volatilization can be carried away with the oxidizing environment flow and deplete the scale from Cr.[17] Further scale protectiveness then relies on the Cr supply from the alloy substrate to the scale.[17] As a result, Fe present at the oxide/alloy interface could diffuse through the vacant lattice sites of Cr in the oxide scale and enhance the formation of a less protective, more Fe-rich Cr_2O_3-based scale.[18,19]

The oxidation and volatilization rates of the Cr_2O_3-based scale is highly dependent on the oxidizing parameters, with higher p_{H_2O}, higher temperature, higher dissolved oxygen content, and increased environment flow rate, increasing the oxidation and volatilization rates.[20] In the case where the environment is not purely steam (e.g. air- H_2O mixture), the oxidation reaction highly depends on the vol.% O_2 and H_2O that exists in the mixture.[1] The calculated vapour pressures of $CrO_2(OH)_2$ for different total steam pressures and air-10% H_2O mixture as a function of temperature shows that a significantly high vapour pressure of $CrO_2(OH)_2$ is produced in air-10% H_2O mixture.[1] It is also shown that the increase in the vol.% H_2O increases the p_{H_2O} that could encourage the Cr_2O_3-based scale breakaway.[1,20]

In the current study, the high-temperature oxidation behavior of the commercial Type 310S stainless steel (~ 24 wt% Cr) is examined in 0.1 MPa and 550 ºC. The 550 ºC temperature is used as it is in the operating temperature range for many H_2O containing environments such as those in steam turbines, low-temperature solid oxide fuel cells, and fuel cladding materials in supercritical water cooled reactors.[21-23] In addition, the importance of the oxidation and volatilization kinetics at the relatively lower 550 ºC temperature is often underestimated and requires further consideration. To examine the effect of p_{H_2O} on the Cr_2O_3-based scale stability and kinetics of the Cr_2O_3-based scale oxidation and volatilization, two environments were chosen with relatively low (air- 10% H_2O) and relatively high (air- 70% H_2O) vol.% H_2O. A more complete physical

description of the Cr_2O_3-based scale volatilization mechanism using the targeted commercial alloy and advanced electron microscopy characterization techniques was obtained. The kinetics of oxidation and volatilization in the two environments was also discussed.

2. Experimental procedures

2.1. Material

Commercial plate of Type 310S stainless steel (Cr: 24.3 wt%, Ni: 19.5 wt%, C: 0.06 wt%, Mn: 1.0 wt%, Si: 0.8 wt%, Mo: 0.8 wt%, and Fe: balance) was solution annealed at 1150 °C for 1 h followed by water quenching to room temperature. Rectangular test coupons with the dimensions of 15 mm × 9.2 mm × 1.5 mm were prepared from the plate using a diamond wheel saw. The provided coupons were then ground to a 400 grit surface finish using SiC abrasive papers with H_2O as a lubricant and cleaned in ethanol. Prior to the coupons exposure in the oxidizing environments, their dimensions and weight were measured using digital caliper and analytical balance, respectively.

2.2. Wet oxidation testing

A 120 cm quartz tube with the inner diameter of 11 mm was fitted inside a 80 horizontal furnace. The temperature inside the quartz tube and at the center of its length was kept at 550 ± 3 ºC. Two exposure conditions were chosen to examine the effect of p_{H2O} on the scale stability: air-10% H_2O and air-70% H_2O. Deionized water was first heated inside a water flask to 46 ºC for the air-10% H_2O test and 90 ºC for the air-70% H_2O test. An air stream was flushed into the heated deionized water flask and the air-x vol.% H_2O mixture flew into the quartz tube with the flow rate of 200 $mL.min^{-1}$ (velocity of 4.2 $cm.s^{-1}$). Five coupons (per exposure time and exposure condition) were then inserted in the center of the quartz tube parallel to the flow direction. Exposure times

considered were 100 h, 250 h, and 500 h. All coupons weights were measured after exposure using the analytical balance with the precision of ± 0.0001 g in order to obtain the amount of weight gained due to oxidation.

2.3. Oxide scale characterization

Scanning electron microscopy (SEM) was initially used for the analysis of the nature and morphology of the oxide scales formed on the coupons in plan-view. This was done using a JEOL JAMP-9500F AUGER/FE-SEM microscope equipped with a Schottky Field Emission Gun (FEG) filament and an integrated Oxford Synergy system with INCA EDS X-ray micro-analysis using an accelerating voltage of 10 kV and a working distance of ~ 20-23 mm. Site-specific TEM thin film specimens were prepared from the coupons exposed for 500 h (the longest exposure time) in each of the environments considered. This was done using Zeiss NVision 40 focused ion beam (FIB) with a Ga ion beam voltage of 30 kV, a current beam of 80 pA and a working distance of 5.6-5.9 mm. To protect the oxide scales during the ion milling, a ~ 200 nm thick C layer first and a ~ 2 μm thick W strap layer next, were deposited on the coupons. TEM analysis was conducted using JEOL 2010F TEM/STEM operating at 200 kV. High resolution TEM (HRTEM) images were obtained from the base scale and the alloys substrate to characterize the structure of the phases present. The very thin oxide scales formed were characterized using Electron Energy Loss Spectroscopy (EELS) with a dispersion of 0.2 eV/channel while the microscope was operated in the high angle annular dark field (HAADF)-Scanning (S)TEM mode. EELS qualitative analysis was obtained by comparing the intensity of a specific energy loss (eV) window to each one of the characteristic edges that is observed in a typical EELS spectrum and the position of these edges as compared to reference materials. For characterizing different types of oxides formed on an austenitic Fe-Cr-Ni alloy, O-K, Cr-$L_{2,3}$, Fe-$L_{2,3}$, and Ni-$L_{2,3}$ edges can all be used for oxide

analysis, however, the O-K edges typically show more variation in each oxide type. **Figure 1** shows the reference EELS spectra [24-29] that were used in the current study as re-plotted using the Plot Digitizer software.[30] The red arrow in **Figure 1(a)** shows the characteristic feature of a spinel oxide structure: a shoulder peak at ~ 550 eV.[29]

3. Results and discussion

Figure 2 shows the weight gain comparison of coupons exposed in 0.1 MPa and 550 ºC flowing air-10% H_2O and air-70% H_2O for up to 500 h. The error bars show the 95% confidence interval for 5 coupons per exposure condition. The weight gain data for the air-10% H_2O test, considering the error bars did not show a noticeable change over the exposure times considered. The oxidation kinetics followed the parabolic rate law with the alloy parabolic rate constant (k_p) of ~ 1.7×10^{-12} $g^2/cm^4.s$. The weight gain data for the air-70% H_2O showed a paralinear kinetics, that is the combination of an initial parabolic kinetic rate law (k_p of ~ 3.5×10^{-13} $g^2/cm^4.s$) followed by a linear kinetic rate law with the alloy negative linear rate constant (k_l) of ~ 2×10^{-12} $g/cm^2.s$. The values measured in this study are comparable with those published in the literature for high Cr-containing Fe-Cr-Ni alloys exposed in air and/or in the presence of H_2O.[2, 31, 32] The k_p value in the air-70% H_2O test was lower than that of the air-10% H_2O due to the lower p_{O_2} (required for the oxide formation) in this environment.

Figure 3 shows plan-view secondary electron images of the coupons surfaces after each of the exposure times and conditions considered. The coupons surfaces in all cases consisted of fine-grained oxide scale. The grinding lines from the surface preparation prior to exposure were noticeable on the surface, implying that the scale had very small (~ few hundred nanometers) thickness. It should be mentioned that small bright particles were randomly detected on the coupons surface after 250 h exposure in air-70% H_2O (**Figure 3[b]**). The SEM-EDS spot analysis

showed that these particles were enriched in Mn and O. The presence of the Mn-enriched oxide particles on the coupon surface could be as the result of the outermost oxide layer breakaway. The similarity in the morphology of the scale formed on coupons in all the exposure times considered implies that the oxidation and volatilization rates in the two environments at 0.1 MPa and 550 ºC is relatively low.

Figure 4(a) and **Figure 4(b)** show the HAADF-STEM cross section images of coupons exposed for 500 h (the longest time) in air-10% H_2O and air-70 % H_2O, respectively. The black and white areas on top of the base scale are the deposited C and W layers, respectively during FIB milling. In both cases, a uniform base scale was formed on the substrate. Recrystallized grains from the surface deformation during the surface preparation were detected below the scale/alloy interface. The base scale thickness in air-10% H_2O was ~ 68 nm compared with that of the ~ 50 nm in air-70% H_2O. The relatively similar scale thickness and small weight gain difference in the two environments as was seen in **Figure 2** suggest the slow oxidation and volatilization rates at 0.1 MPa and 550 ºC.

Figure 5 shows the cross-section HAADF-STEM image and Fe, Cr, Mn, Ni, and O EELS elemental maps of the base scale formed after 500 h exposure in air-10% H_2O. The black and white areas on top of the base scale in the HAADF-STEM image are the deposited C and W layers, respectively during FIB milling. The base scale was enriched in Cr and Mn. **Figure 6** shows the corresponding EELS spectra from *Areas* 1, 2, and 3 in **Figure 5**. The base scale was characterized as Cr_2O_3 layer with small Fe dissolved in it (*Areas* 1 and 3). The Mn-enriched layer on top of the Cr_2O_3 layer was characterized as $MnCr_2O_4$ (*Area* 2). The formation of a spinel $MnCr_2O_4$ layer on the Cr_2O_3 layer is well established in Mn containing stainless steels because of the high Mn diffusivity in the Cr_2O_3 layer.[33] It has been shown that a $MnCr_2O_4$ cap on the Cr_2O_3 layer could

positively affect the volatilization rate of the base scale in that the Cr loss rate from a $MnCr_2O_4$ layer is much less than that of the Cr_2O_3 layer.[34]

Figure 7 shows the cross-section HAADF-STEM image and the Fe, Cr, Mn, Ni, and O EELS elemental maps of the base scale formed after 500 h exposure in air-70% H_2O. The corresponding EELS spectra from areas in the HAADF-STEM image are shown in **Figure 8**. The black and white areas on the base scale in the HAADF-STEM image are the deposited C and W layers, respectively during FIB milling. The base scale was enriched in Cr and Mn. The base scale was characterized as Cr_2O_3 layer (*Area* 4). The Mn-enriched layer on top of the Cr_2O_3 layer was identified as $MnCr_2O_4$ (*Area* 5). *Area* 6 contained more Mn, and was identified as MnO.

It has been shown that Cr loss in the presence of H_2O, could also occur from a $MnCr_2O_4$ layer (equation 2):[34]

$$\frac{1}{2}MnCr_2O_{4_{(s)}} + H_2O_{(g)} + \frac{3}{4}O_{2_{(g)}} = CrO_2(OH)_{2_{(g)}} + \frac{1}{2}MnO_{(s)} \quad (2)$$

The physical evidence of MnO deposition on the Cr_2O_3 layer as was seen in this study **(Figure 3(b)** and **Figure 7)**, after 500 h exposure of coupons in air-70% H_2O, supports the aforementioned thermodynamic theory.

Figure 9 shows the cross-section HAADF-STEM image of the alloy after 500 h exposure in air-70% H_2O and the EELS spectra from the corresponding points shown in the image. Points 1-6 EELS spectra were obtained where the Cr loss from the $MnCr_2O_4$ resulted in the MnO deposition on the oxide surface and transformation of $MnCr_2O_4$ into a $Mn_xCr_{2y}O_4$ layer. Points 7-12 EELS spectra were obtained adjacent to points 1-6 for comparison. In points 1-6, the Cr-$L_{2,3}$ peaks in the base scale decreased from the alloy-oxide interface to the oxide-air-70% H_2O interface, which confirmed the Cr depletion from the oxide surface due to base scale volatilization. In the

meanwhile, the Mn-$L_{2,3}$ peak increased from the alloy-oxide interface to the oxide-air-70% H_2O interface (points 1-6). Complete disappearance of Cr-$L_{2,3}$ peaks while Mn-$L_{2,3}$ peaks were still present at the oxide- air-70% H_2O interface, confirmed the volatilization of Cr from a $MnCr_2O_4$ layer and deposition of MnO, which is in agreement with the previously published thermodynamic theory.[34] The adjacent points 7-12 on the other hand, showed that the $MnCr_2O_4$ layer stayed intact on top of the Cr_2O_3 layer. Very small amount of Fe was dissolved in the $MnCr_2O_4$ layer. This suggests that the Cr loss from the $MnCr_2O_4$ layer and deposition of MnO, also Fe dissolution in the $MnCr_2O_4$ layer on the surface, are localized phenomena.

Figure 10 shows the HRTEM image of the alloy/oxide interface after 500 h exposure of coupons in both environments. The EELS spectra corresponding to the amorphous layers are shown in **Figure 10(b)** and **Figure 10(d).** In both environments after 500 h exposure, a ~ 5 nm thick oxide layer was seen at the scale/alloy interface which was characterized as SiO_2 layer. Formation of a SiO_2 layer below the base scale in stainless steels during oxidation is very common. The thickness of this layer, however, depends on the Si concentration in the alloy, temperature, pressure and exposure time.[35] It is known that the SiO_2 layer might positively enhance the oxidation rate of the alloys at high temperatures by reducing ions diffusion through the scale.[35] The protective SiO_2 layer thickness is believed to be ~ 1 µm therefore the ~ 5 nm thick SiO_2 layer observed in this study does not seem to play a role in protectiveness of the alloy against high-temperature oxidation.[35]

Figure 11 shows the summary of the scales characterization after 500 h exposure in 0.1 MPa and 550 ºC air-10% H_2O and air-70% H_2O. The ~ 5 nm SiO_2 layer underneath the base scale is not shown and the scales thicknesses are not set to scale. In both cases, a $MnCr_2O_4$ oxide cap formed on top of the Cr_2O_3 layer. The Cr loss rate is known to be much less from the $MnCr_2O_4$ layer

compared with that of the Cr_2O_3 layer,[34] which is responsible for the small weight gain values obtained in this study and effective protection of the Cr_2O_3-based scale against breakaway. With increase of the p_{H_2O}, the kinetics of the reactions changed from parabolic in air-10% H_2O to paralinear in air-70% H_2O. While the Cr_2O_3-based scale remained protected against volatilization in both environments, the Cr loss from the $MnCr_2O_4$ cap was higher in air-70% H_2O. The physical evidence of MnO deposition as a result of Cr loss from the $MnCr_2O_4$ layer (equation 2, **Figure 3(b)** and **Figure 7**) in air-70% H_2O environment, confirms that the higher p_{H_2O} increased the Cr loss rate from the $MnCr_2O_4$ layer. Not to mention, further study on the Mn-O enriched particles observed in Figure 3(b) is suggested. It should be noted that the Mn and Cr concentration below MnO was different than the areas without MnO. This is shown in **Figure 11** as $Mn_xCr_{2y}O_4$. Results from this work show that in the presence of the $MnCr_2O_4$ layer in the 0.1 MPa pressure and 550 ºC air-10% H_2O and air-70% H_2O, the volatilization rate of the base scale was reduced enormously and Cr_2O_3-based scale breakaway and Fe-rich oxide nodules formation was inhibited.

4. Conclusions

The effect of H_2O presence on the oxidation and volatilization mechanisms of commercial Type 310S stainless steel was examined in air-x vol.% H_2O at 0.1 MPa and 550 ºC. Comparison of the base scales formed in air-10% H_2O and air-70% H_2O environments, showed that the kinetics of oxidation was different in the two environments: parabolic in air-10% H_2O and paralinear in air-70% H_2O. The transition of oxidation kinetics was attributed to the higher volatilization rate of the scale formed in air-70% H_2O. It was shown that the presence of a $MnCr_2O_4$ on top of the Cr_2O_3-based scale reduced the Cr_2O_3 layer volatilization rate and inhibited the scale breakaway from formation of Fe-enriched nodules in both environments for up to 500 h. The relatively higher Cr loss rate from the $MnCr_2O_4$ in the higher p_{H_2O} environment (air-70% H_2O) however, was

responsible for the transition of kinetics from parabolic to paralinear rates, therefore, the vapour pressure of the volatile species for the minor alloying elements are important and must not be underrated.

5. Acknowledgements

The authors acknowledge the funding from Natural Sciences and Engineering Research Council of Canada under the Discovery Grants program. The authors also thank the staff in the Canadian Centre for Electron Microscopy (CCEM), a national facility supported by NSERC, the Canada Foundation for Innovation under the MSI program and McMaster University, for their technical assistance with sample preparation and electron microscopy.

6. References

1. I.G. Wright and R.B. Dooley: "A review of the oxidation behaviour of structural alloys in steam", Int. Mater. Rev., 2010, **55**, 129–167.

2. N. Otsuka and H. Fujikawa: "Scaling of austenitic stainless steels and nickel-based alloys in high-temperature steam at 973 K", Corrosion, 1991, **47**, 240–248.

3. J. Stringer and I.G. Wright: "Current limitations of high-temperature alloys in practical applications", Oxid. Met., 1995, **44**, 265–308.

4. W.H. Yeo, A.T. Fry, J. Purbolaksono, S. Ramesh, J.I. Inayat-Hussain, H.L. Liew, and M. Hamdi, "Oxide scale growth and presumed exfoliation in a 700 °C or higher steam condition: A simulation study for future operations of ultra-supercritical power plants", J. Supercrit. Fluids, 2014, **92**, 215–222.

5. Z. Shao, and S.M. Haile: "A high-performance cathode for the next generation of solid-oxide fuel cells", Nature, 2004, **431**, 170–173.

6. Z. Shen, L. Zhang, R. Tang, and Q. Zhang: "SCC susceptibility of type 316Ti stainless steel in supercritical water", J. Nucl. Mater., 2015, **458**, 206–215.

7. S.N. Karlsdottir, K.R. Ragnarsdottir, I.O. Thorbjornsson, and A. Einarsson: "On-site errosion-corrosion testing in superheated geothermal steam", Geothermics, 2015, **53**, 281–290.

8. Y. Alipour, P. Henderson, and P. Szakálos: "The effect of a nickel alloy coating on the corrosion of furnace wall tubes in a waste wood fired power plant", Mater. Corros., 2014, **65**, 217–225.

9. M. Lukaszewicz, N.J. Simms, T. Dudziak, and J.R. Nicholls: "Effect of steam flow rate and sample orientation on steam oxidation of ferritic and austenitic stainless steels at 650 ºC and 700 ºC", Oxid. Met., 2013, **79**, 473–483.

10. R. Peraldi and B.A. Pint: "Effect of Cr and Ni contents on the oxidation behavior of ferritic and austenitic model alloys in air with water vapor", Oxid. Met., 2004, **61**, 463–483.

11. N. Otsuka, Y. Shida, and H. Fujikawa: "Internal-external transition for the oxidation of Fe-Cr-Ni austenitic stainless steels in steam", Oxid. Met., 1989, **32**, 13–45.

12. M. Lukaszewicz, N.J. Simms, T. Dudziak, and J.R. Nicholls: "Characterisation of oxide scales developed on high temperature resistant alloys in pure steam environments", Mater. High Temp., 2012, **29**, 210–218.

13. A. Yamauchi, K. Kurokawa, and H. Takahashi: "Evaporation of Cr_2O_3 in atmospheres containing H_2O", Oxid. Met, 2003, **59**, 517–527.

14. E.J. Opila, D.L. Myers, N.S. Jacobson, I.M.B. Nielsen, D.F. Johnson, J.K. Olminsky, and M.D. Allendor: "Theoretical and experimental investigation of the thermochemistry of $CrO_2(OH)_2$ (g)", J. Phys. Chem. A, 2007, **111**, 1971–1980.

15. S.I. Castañeda, and F.J. Pérez: "Microstructure and volatile species determination of ferritic/martensitic FB_2 steal in contact with Ar + 40% H_2O at high temperatures", Oxid. Met., 2013, **79**, 147–166.

16. N. Mu, K.Y. Jung, N.M. Yanar, G.H. Meier, F.S. Pettit, and G.R. Holcomb: "Water vapor effects on the oxidation behavior of Fe-Cr and Ni-Cr alloys in atmospheres relevant to oxy-fuel combustion", Oxid. Met., 2012, **78**, 221–237.

17. H. Asteman, J.E. Svensson, and L.G. Johansson: "Evidence of chromium evaporation influencing the oxidation of 304L: the effect of temperature and flow rate", Oxid. Met., 2002, **57**, 193–216.

18. D.J. Young and B. A. Pint: "Chromium volatilization rates from Cr_2O_3 scales into flowing gases containing water vapor", Oxid. Met., 2006, **66**, 137–153.

19. M. Halvarsson, J.E. Tang, H. Asteman, J.E. Svensson, and L.G. Johansson: "Microstructural investigation of the breakdown of the protective oxide scale on a 304 steel in the presence of oxygen and water vapour at 600 ºC", Corros. Sci., 2006, **48**, 2014–2035.

20. H. Asteman, J. Svensson, M. Norell, and L. Johansson: "Influence of water vapor and flow rate on the high-temperature oxidation of 304L; effect of chromium oxide hydroxide evaporation", Oxid. Met., 2000, **54**, 11—26.

21. Alina Agu¨ero , Rau´l Muelas, Ana Pastor, Steve Osgerby: "Long exposure steam oxidation testing and mechanical properties of slurry aluminide coatings for steam turbine components", Surface and Coatings Technology, 2005, **200**, 1219 – 1224.

22. Eric D. Wachsman and Kang Taek Lee: "Lowering the temperature of solid oxide fuel cells", Science, 2011, **334**, 935-939.

23. S. Mahboubi, Y. Jiao, W. Cook, W. Zheng, D. Guzonas, G.A. Botton and J.R. Kish: "Stability of chromia (Cr_2O_3)-based scales formed during corrosion of austenitic Fe-Cr-Ni alloys in flowing oxygenated supercritical water", Corrosion, 2016, **72**, 1170-1180.

24. Y. Chen, Z. Liu, S. P. Ringer, Z. Tong, X. Cui, and Y. Chen: "Selective Oxidation Synthesis of $MnCr_2O_4$ Spinel Nanowires from Commercial Stainless Steel Foil", Crystal Growth and Design, 2007, **7**, 2279-2281.

25. J. Bischoff and A.T. Motta: "EFTEM and EELS analysis of the oxide layer formed on HCM12A exposed to SCW", J. Nucl. Mater. 2012, **430**, 171–180.

26. H.K. Schmid and W. Mader: "Oxidation states of Mn and Fe in various compound oxide systems", Micron, 2006, **37**, 426–432.

27. H. Kurata and C. Colliex: "Electron-energy-loss core-edge structures in manganese oxides", Phys. Rev. B, 1993, **48**, 2102–2108.

28. G.A. Botton, C.C. Appel, A. Horsewell, and W.M. Stobbs: "Quantification of the EELS near-edge structures to study Mn doping in oxides", J. Microsc., 1995, **180**, 211–216.

29. S. Mahboubi: "Effect of Cr content on corrosion resistance of Fe-Cr-Ni alloys exposed in supercritical water (SCW)", M.A.Sc. thesis, McMaster Univeristy, 2014.

30. "Plot Digitizer Software", http://sourceforge.net/projects/plotdigitizer/.

31. A. Pau´l, R. Sa´nchez, O. M. Montes, and J. A. Odriozola: "The role of silicon in the reactive-elements effect on the oxidation of conventional austenitic stainless steel", Oxid. Met., 2007, **67**, 87–105.

32. B.A. Pint, K.A. Terrani, M.P. Brady, T. Cheng, J.R. Keiser: "High temperature oxidation of fuel cladding candidate materials in steam-hydrogen environment", J. Nucl. Mater., 2013, **440**, 420–427.

33. A.C.S. Sabioni, A.M. Huntz, L.C. Borges, and F. Jomard: "First study of manganese diffusion in Cr_2O_3 polycrystals and thin films by SIMS", Philos. Mag., 2007, **87**, 1921–1937.

34. G.R. Holcomb and D.E. Alman: "The effect of manganese additions on the reactive evaporation of chromium in Ni-Cr alloys", Scr. Mater., 2006, **54**, 1821–1825.

35. H.E. Evans, D.A. Hilton, R.A. Holm, and S.J. Webster, "Influence of silicon additions on the oxidation resistance of a stainless steel", Oxidation of Metals, 1983, **19**, 1-18.

List of Figures:

Figure 1. EELS spectra in reference compounds for a) Cr_2O_3 and $MnCr_2O_4$, and b) MnO, MnO_2, Mn_2O_3, Mn_3O_4.[24-29] The red arrow in (a) shows the characteristic feature of a spinel $MnCr_2O_4$ structure.

Figure 2. Weight gain data of coupons exposed in 0.1 MPa and 550 ºC air-10% H_2O and air-70% H_2O for up to 500 h. The error bars show the 95% confidence interval for 5 coupons per data point.

Figure 3. Plan-view secondary electron images of coupons exposed in 0.1 MPa and 550 ºC air-10% H_2O and air-70% H_2O for up to 500 h.

Figure 4. Cross-section HAADF-STEM images of coupons after 500 h exposure in 0.1 MPa and 550 ºC (a) air-10% H_2O and (b) air-70% H_2O for 500 h.

Figure 5. Cross-section HAADF-STEM image and EELS Fe, Cr, Mn, Ni, and O elemental maps of the base scale formed on Type 310S stainless steel after 500 h exposure in 0.1 MPa and 550 ºC air-10% H_2O.

Figure 6. EELS spectra of *Areas* 1, 2, and 3 in the HAADF-STEM image in Figure 5.

Figure 7. Cross-section HAADF-STEM image and EELS Fe, Cr, Mn, Ni, and O elemental maps of the base scale formed on Type 310S stainless steel after 500 h exposure in 0.1 MPa and 550 ºC air-70% H_2O.

Figure 8. EELS spectra of *Areas* 1, 2, and 3 in the HAADF-STEM image in Figure 7.

Figure 9. (a) Cross-section HAADF-STEM image of Type 310S stainless steel after 500 h exposure in 0.1 MPa and 550 ºC air-70% H_2O, (b) the corresponding EELS spectra from points 1-6 in (a), and (c) the corresponding EELS spectra from points 7-12 in (a).

Figure 10. HRTEM images of the alloy/oxide interface and the EELS spectra of the amorphous regions (obtained in DF-STEM mode), in Type 310S stainless steel after 500 h exposure in 0.1 MPa and 550 ºC air-10% H_2O (a) and (b), and air-70% H_2O (c) and (d).

Figure 11. Summary of the scale characterization after 500 h exposure of Type 310S stainless steel coupons in 0.1 MPa and 550 ºC air-10% H_2O and air-70% H_2O.

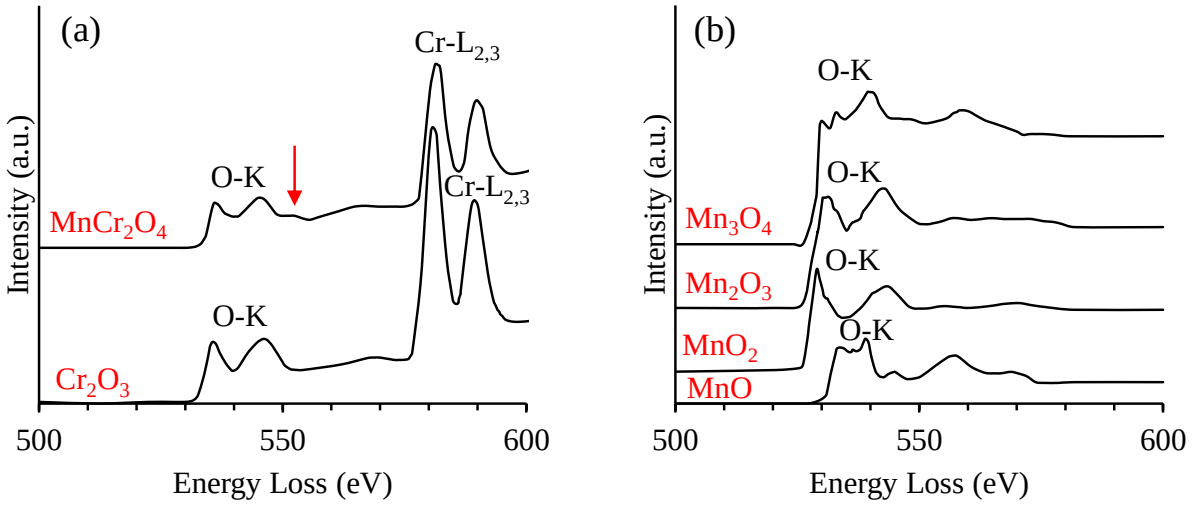

Figure 1. EELS spectra in reference compounds for a) Cr_2O_3 and $MnCr_2O_4$, and b) MnO, MnO_2, Mn_2O_3, Mn_3O_4.[24-29] The red arrow in (a) shows the characteristic feature of a spinel $MnCr_2O_4$ structure.

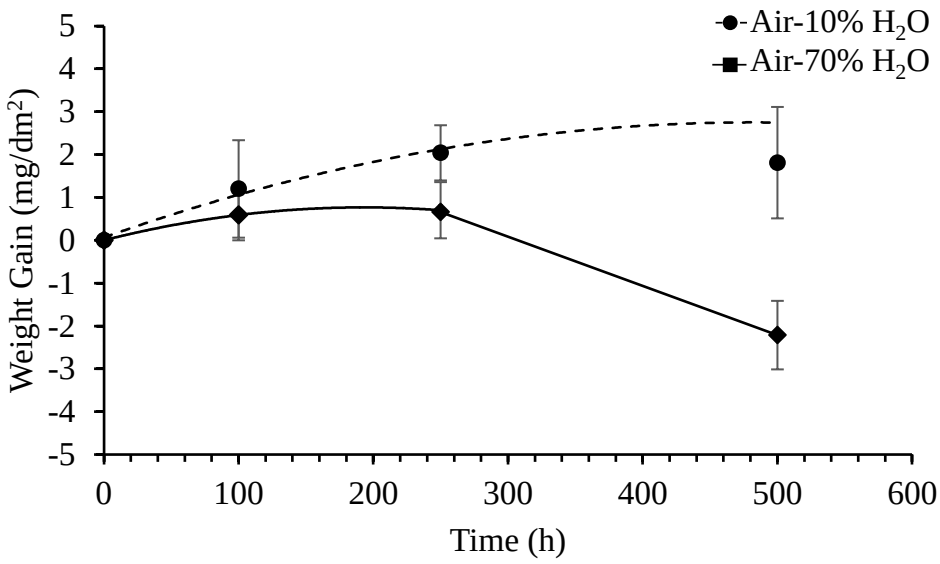

Figure 2. Weight gain data of coupons exposed in 0.1 MPa and 550 ºC air-10% H_2O and air-70% H_2O for up to 500 h. The error bars show the 95% confidence interval for 5 coupons per data point.

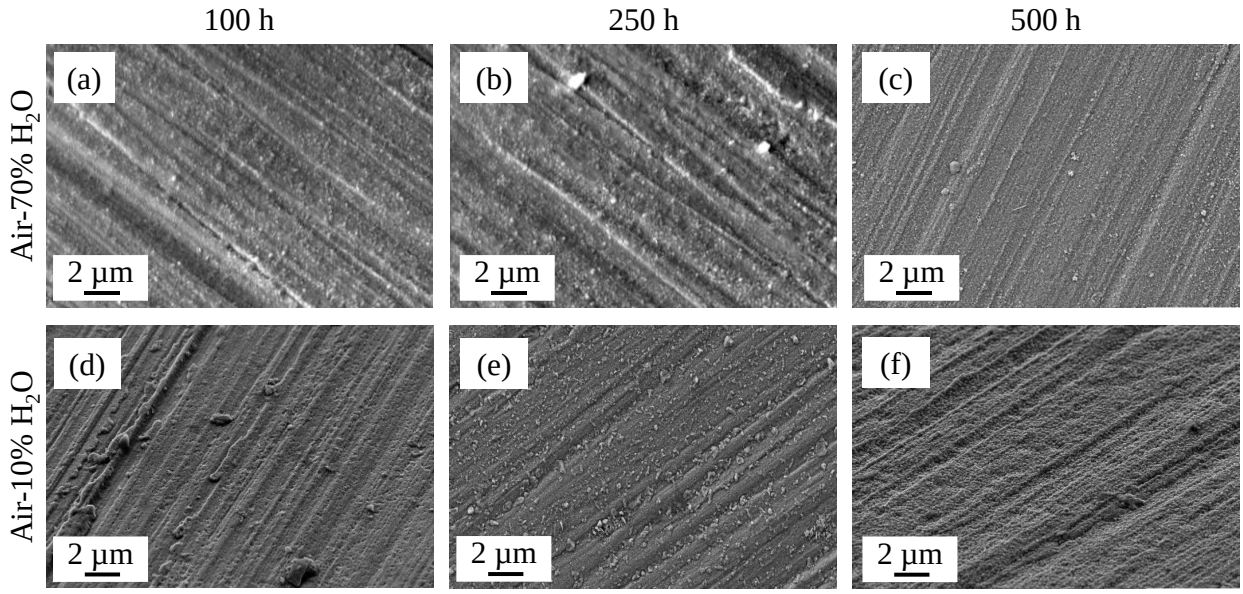

Figure 3. Plan-view secondary electron images of coupons exposed in 0.1 MPa and 550 ºC air-10% H_2O and air-70% H_2O for up to 500 h.

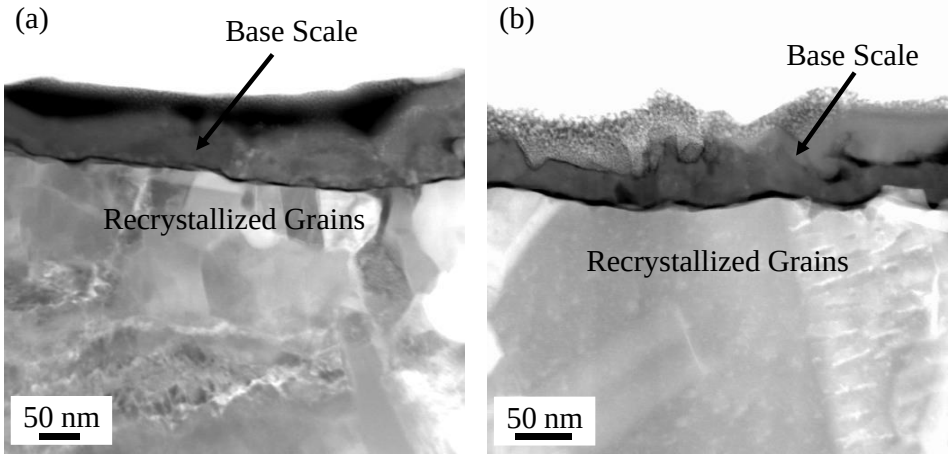

Figure 4. Cross-section HAADF-STEM images of coupons after 500 h exposure in 0.1 MPa and 550 ºC (a) air-10% H_2O and (b) air-70% H_2O for 500 h.

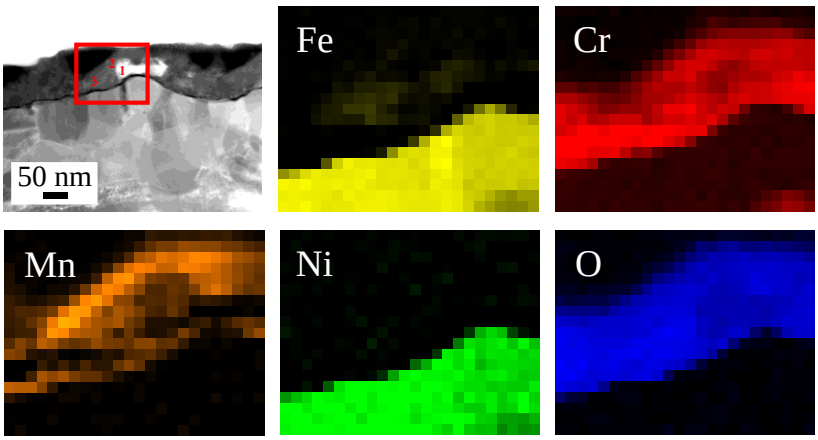

Figure 5. Cross-section HAADF-STEM image and EELS Fe, Cr, Mn, Ni, and O elemental maps of the base scale formed on Type 310S stainless steel after 500 h exposure in 0.1 MPa and 550 ºC air-10% H_2O.

(a)

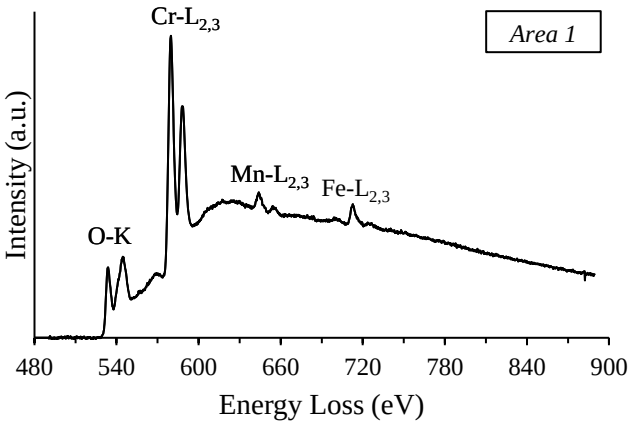

(b)

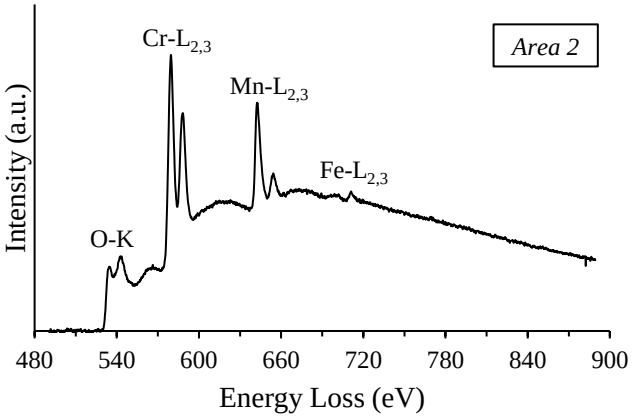

(c)

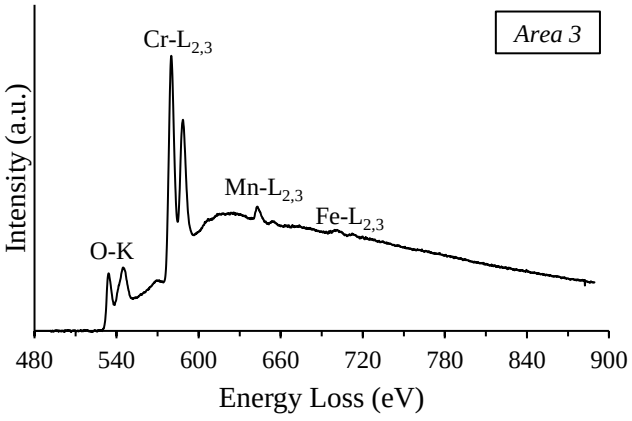

Figure 6. EELS spectra of *Areas* 1, 2, and 3 in the HAADF-STEM image in Figure 5.

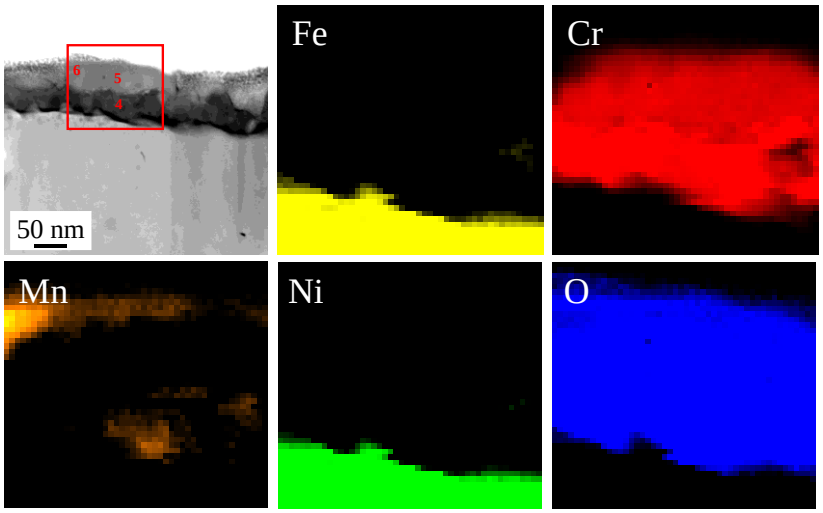

Figure 7. Cross-section HAADF-STEM image and EELS Fe, Cr, Mn, Ni, and O elemental maps of the base scale formed on Type 310S stainless steel after 500 h exposure in 0.1 MPa and 550 ºC air-70% H_2O.

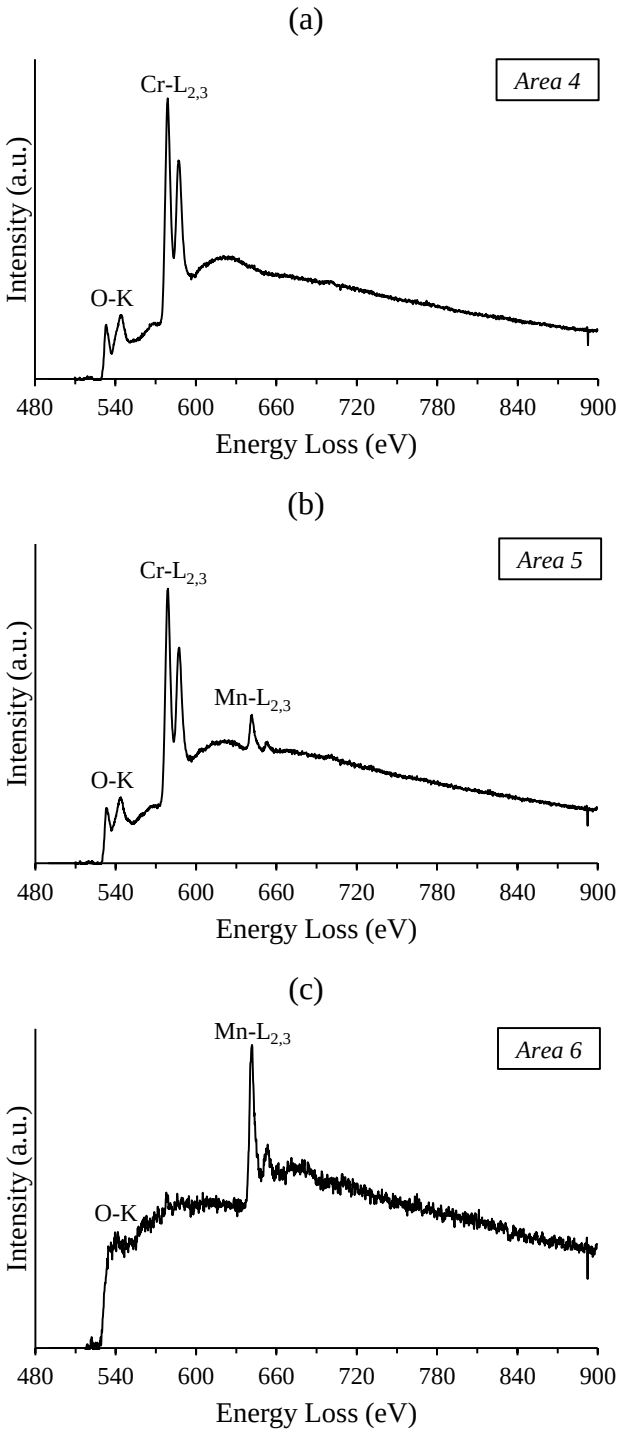

Figure 8. EELS spectra of *Areas* 1, 2, and 3 in the HAADF-STEM image in Figure 7.

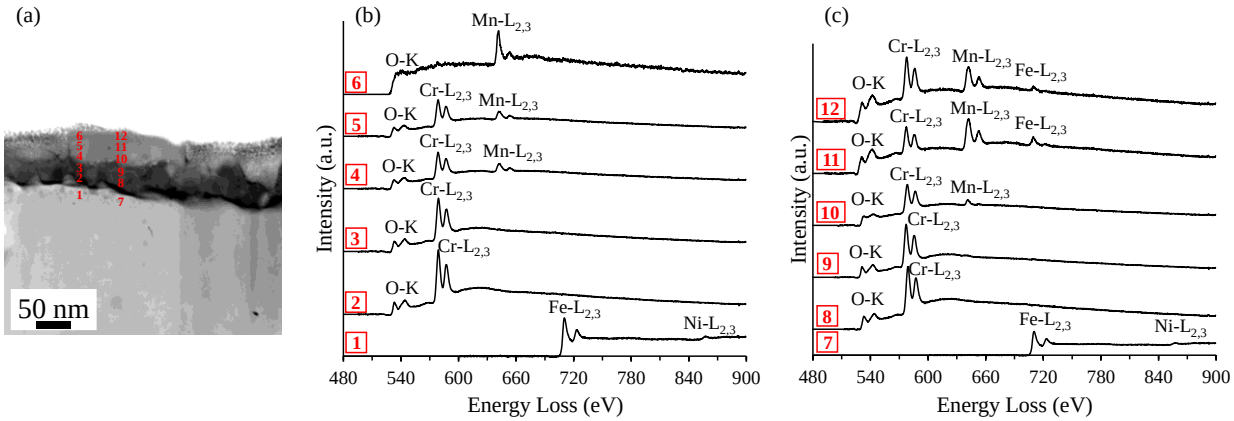

Figure 9. (a) Cross-section HAADF-STEM image of Type 310S stainless steel after 500 h exposure in 0.1 MPa and 550 ºC air-70% H_2O, (b) the corresponding EELS spectra from points 1-6 in (a), and (c) the corresponding EELS spectra from points 7-12 in (a).

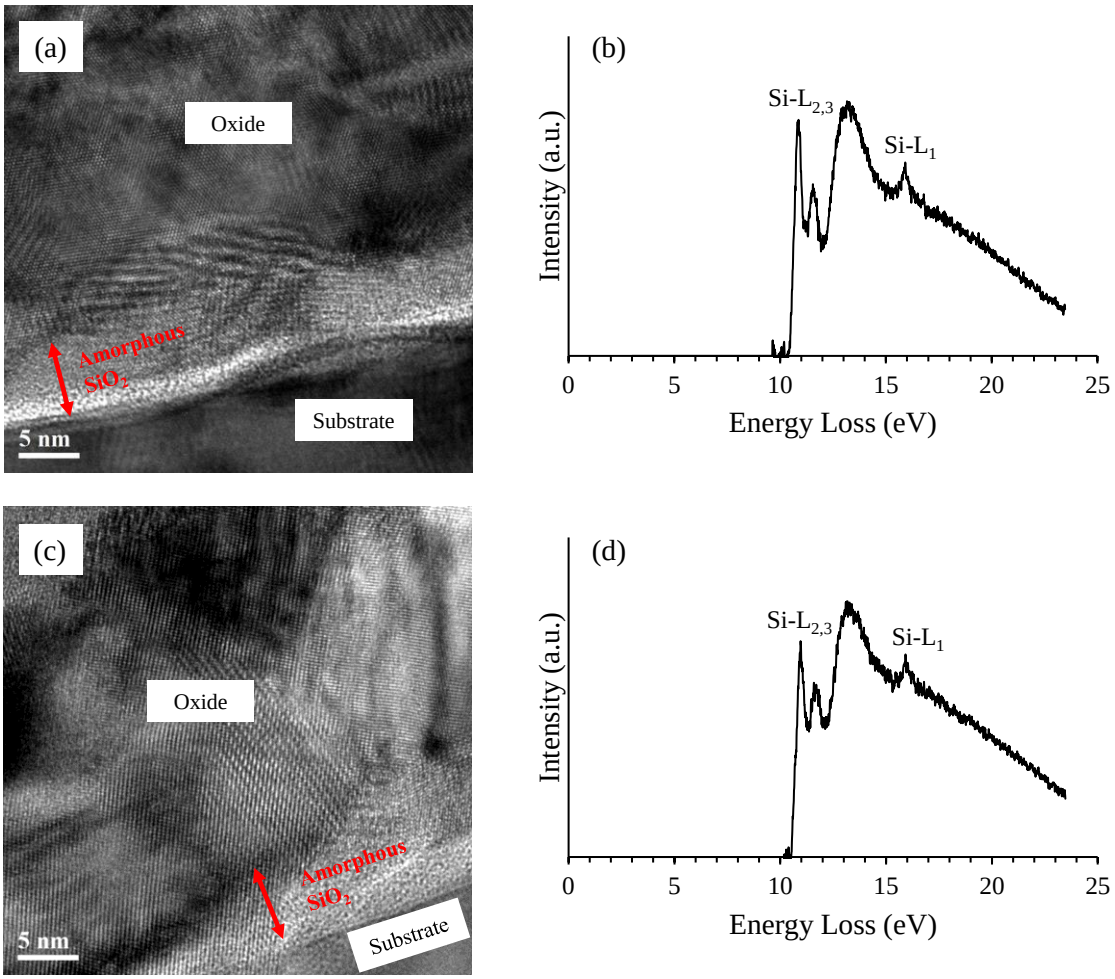

Figure 10. HRTEM images of the alloy/oxide interface and the EELS spectra of the amorphous regions (obtained in DF-STEM mode), in Type 310S stainless steel after 500 h exposure in 0.1 MPa and 550 ºC air-10% H_2O (a) and (b), and air-70% H_2O (c) and (d).

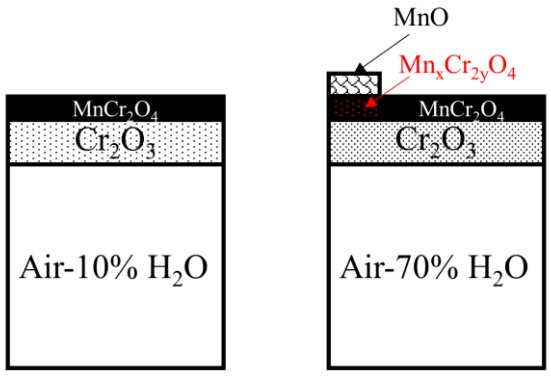

Figure 11. Summary of the scale characterization after 500 h exposure of Type 310S stainless steel coupons in 0.1 MPa and 550 ºC air-10% H_2O and air-70% H_2O.